7th ECCOMAS Thematic Conference on Smart Structures and Materials
SMART 2015
A.L. Araúo, C.A. Mota Soares, et al. (Editors)

ACTIVE CONTROL OF THE PASSIVE PITCHING OF A FLAPPING WING WITH ELECTROSTATIC CLAMPING

Hugo J. Peters[⋆♮], Qi Wang[⋆], Johannes F.L. Goosen[⋆] and Fred van Keulen[⋆]

[⋆] Structural Optimization & Mechanics, Department of Precision and Microsystems Engineering,
Faculty of Mechanical, Maritime and Materials Engineering, Delft University of Technology
Mekelweg 2, 2628 CD Delft, The Netherlands
{h.j.peters-1, q.wang-3, j.f.l.goosen, a.vankeulen}@tudelft.nl

[♮]DevLab, Development Laboratories
Horsten 1, MMP 0.10, 5612 AX Eindhoven, The Netherlands

Keywords: passive pitching control, electrostatically controlled device, large deformations, non-linear behavior, FWMAV.

Summary: *Wing designs for Flapping Wing Micro Air Vehicles (FWMAVs) might use a properly tuned elastic hinge at the wing root to obtain the required passive pitching motion to stay aloft. Practical use of this type FWMAVs requires some form of control which can be achieved by actively adjusting the elastic hinge stiffness and, thus, the pitching motion and lift production of the wing. This paper introduces an elastic hinge design consisting of stacked layers which can be clamped together using an electrostatic loading. This clamping changes the bending stiffness of the hinge. The voltage dependent characteristics of this elastic hinge during the large pitching motion are described in detail. A quasi-steady aerodynamic model is used to obtain the equation of motion of the passive pitching flapping motion as a function of the elastic hinge stiffness and the applied control voltage. Numerical simulations show significant changes of the passive pitching motion and of the lift production, if the layers are clamped together. Experiments are conducted to study the practical applicability of this method for FWMAV applications. The experiments show similar trends although the effect is less significant which is mainly due to manufacturing difficulties. In conclusion, this method is promising in controlling FWMAV designs.*

1 INTRODUCTION

The design and realization of lightweight Flapping Wing Micro Air Vehicles (FWMAVs) have attracted much attention over the last decades. Potential applications of FMWAV designs are in, among others, surveillance (e.g., police and security) and inspection of inaccessible or dangerous locations (e.g., disaster scenes and sewers). The design and realization of FWMAVs is complicated by constraints on weight and power consumption as determined by the limited lift production of the wings. Consequently, designers aim for lightweight, smart and highly integrated structures. This has resulted in several ways of achieving flapping kinematics for

sufficient lift production. To decrease the actuation mechanism complexity, some wing designs integrate an elastic hinge that allows the wing pitching motion to be passive during the flapping motion [1, 2]. Due to the inertial and aerodynamic loading, a properly tuned elastic hinge results the required pitching motion to achieve the lift to stay aloft.

For stable flight and maneuvering, FWMAV designs require some form of control. In fact, constant control will be necessary because of the intrinsic dynamic instability of the designs. Recent work on the Harvard Microrobotic Fly (i.e., a FWMAV design which exploits passive pitching) applied aerodynamic dampers for stabilization [3], complex mechanisms to induce asymmetric flapping wing kinematics to produce control torques [4], and separate actuators for each wing [5]. Additionally, control torques were created by integrating a piezoelectric bimorph actuator in the wings' elastic hinge to induce a bias during the wing stroke [6]. To control lightweight FWMAV designs, actively adjusting the dynamic properties (i.e., structural damping and stiffness) of the wings' elastic hinge appears to be a promising, elegant, and integrable approach to change the passive pitching motion during flight and, hence, the stroke averaged lift force. This control approach is not well established within literature.

To actively change the dynamic properties of the wings' hinge, the elastic hinge needs to be replaced by an active hinge which properties change due to some external stimuli (e.g., an electric field). There are several methods to actively change the dynamic properties of an elastic element: I) with smart fluids (i.e., magnetorheological or electrorheological fluids) for which the properties transform rapidly upon exposure to an external magnetic or electric field [7], II) with piezoelectric polymer films (e.g., PVDF) for which the properties change as a function of the connected electrical circuit [8], or III) by clamping stacked layers to each other using, for example, electrostatic forces [9, 10].

The latter method, shown in Figure 1, is investigated in this paper. Figure 1a shows a capacitor-like clamped-free beam which consists of two sandwich layers which can slide with respect to each other when deflected by the end-load F. The sandwich layers consist of a conducting layer (e.g., steel) and a dielectric layer (e.g., Mylar). Figure 1b shows that, during deflection, the two sandwich layers slide with respect to each other if the applied voltage $V = 0$. For a specific voltage V_{cl}, the electrostatic loading causes the sandwich layers to be clamped to each other during deflection, see Figure 1c. Whenever these layers are clamped, the area moment of inertia increases which, effectively, increases the bending stiffness of the beam.

This work aims to actively control the wing's passive pitching motion using electrostatic clamping of stacked layers. This active hinge needs to be integrated into the lightweight wing design (i.e., about 200 mg) and should allow for large passive pitching deflections. This work investigates the influence of an electrostatic load on the dynamic properties of the active hinge during these large deflections. We assume the wing to be a thin, rigid plate for simplicity reasons. This work uses a quasi-steady aerodynamic model to obtain the equation of motion of the passive pitching flapping motion as a function of the elastic hinge properties. Experiments are conducted to study the practical applicability of this active element for small-scale and lightweight FWMAV applications.

This paper is organized as follows: Section 2 shows the passive pitching motion during a

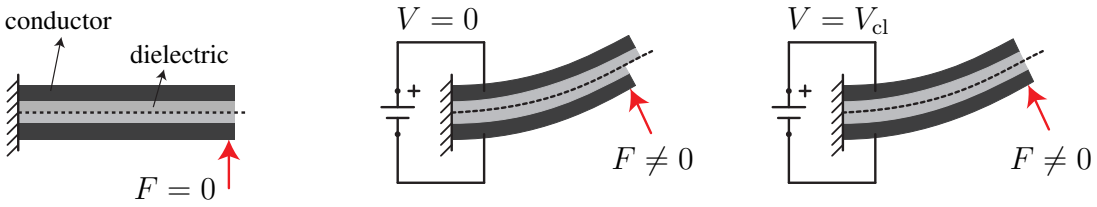

(a) Capacitor-like clamped-free beam with end-load F to deflect the beam.

(b) For $V = 0$, the layers are sliding with respect to each other during deflection.

(c) For $V = V_{\text{cl}}$, the layers are clamped together: effectively increasing the bending stiffness.

Figure 1: Conceptual idea to change the bending stiffness of a clamped-free beam with end-load F which consists of two stacked conductor-isolator sandwich layers by clamping the layers using an electrostatic load.

flapping cycle and the relation to the aerodynamic performance. The theory about the electrostatically controlled structural properties of the elastic hinge is discussed in Section 3. Section 4 presents the equation of motion of a passive pitching flapping wing based on a quasi-steady aerodynamic model. The active hinge is integrated in this model to study the passive pitching motion as a function of the electrostatic load. Section 5 discusses the realization of the active hinge, the experimental setup, the obtained measurement results, and the comparison with the analytical results. Section 6 gives conclusions and recommendations for further research.

2 PASSIVE PITCHING FLAPPING MOTION

2.1 Flapping wing design

Both insects and FWMAVs show flapping wings with different outlines, stiffness distributions and materials. The pitching motion is, generally, generated passively with the help of wing flexibility. This wing flexibility is, for instance, realized with: I) a flexible veins-membrane structure as known from insect wings, II) a carbon-fiber-reinforced polymer film as commonly used in FWMAV wing designs, or III) with an elastic hinge at the wing root to represent the wing stiffness. This work uses the latter approach which is generally used for experimental studies.

Figure 2 shows the wing design as studied in this work consisting of a rectangular, thin plate which is assumed to be rigid with an elastic hinge at the wing root. The wingspan and chord length are denoted by R and c, respectively. The elastic hinge has a width b, a length L and a thickness t. This elastic hinge is essentially a compliant hinge, which is primarily loaded in bending. The effective rotational stiffness can, consequently, be given by [11]:

$$k_{\text{rot}} = \frac{EI}{L}, \tag{1}$$

where E and I are the Young's modulus and cross sectional area moment of inertia of the hinge. For pure bending, this simple equation is still accurate for large deflections.

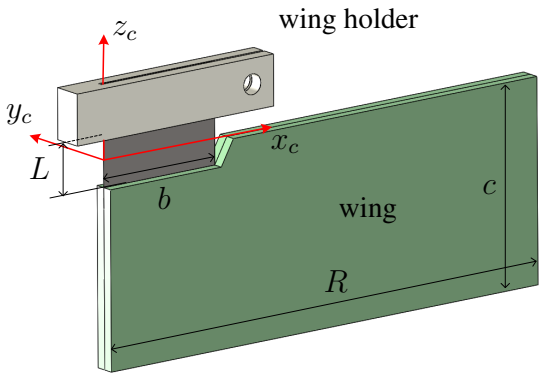

Figure 2: Schematic drawing of the wing design with the elastic hinge connecting the wing holder to the wing.

2.2 Passive pitching and wing performance

Flapping wing motion is a spatial wing movement that can be decomposed into three successive motions, namely sweeping motion (or yaw), pitching motion (or pitch), and heaving motion (or roll). The sweeping motion drives the wing to sweep reciprocally in a stroke plane with a specified stroke amplitude. The pitching motion controls the geometrical angle of attack (AOA) of the flapping wings. For flapping wings, the highest AOA (i.e., $90°$) is, generally, experienced during wing reversal phases while the lowest AOA shows up during the middle of the strokes. The heaving motion represents the out-of-stroke-plane movement whose amplitude is generally one order smaller than the other two motions. Hence, it is ignored in this study. For the current wing design model, the flapping kinematics can be fully determined by the sweeping motion and the pitching motion.

Two Euler angles are used to quantify the wing kinematics: the sweeping angle ϕ, and the pitching angle η. Additionally, we specify two coordinate frames which are of particular interest for the study of flapping wing motion: the fixed inertial frame $x_i y_i z_i$ and the co-rotating frame $x_c y_c z_c$ which is fixed to the wing and shown in Figure 2. The angular velocity and acceleration of a flapping wing in the co-rotating frame can be expressed by

$$\boldsymbol{\omega}_c = \dot{\phi}\boldsymbol{R}_\eta^T \boldsymbol{R}_\phi^T \boldsymbol{e}_{z_i} + \dot{\eta}\boldsymbol{e}_{x_c} = \left[\dot{\eta}, \dot{\phi}\sin(\eta), \dot{\phi}\cos(\eta)\right]^{\mathrm{T}}, \quad \text{and} \tag{2}$$

$$\boldsymbol{\alpha_c} = \dot{\boldsymbol{\omega}}_c = \left[\ddot{\eta}, \dot{\phi}\dot{\eta}\cos(\eta) + \ddot{\phi}\sin(\eta), \ddot{\phi}\cos(\eta) - \dot{\phi}\dot{\eta}\sin(\eta)\right]^{\mathrm{T}}, \tag{3}$$

respectively, where $\boldsymbol{R}_\phi$ and $\boldsymbol{R}_\eta$ are rotation matrices representing the sweeping and pitching motions, respectively. For a given AOA and mass distribution of the wing, the inertial and aerodynamic load can be fully determined if Eqs. (2) and (3) are known. The AOA can be simply obtained by $\|90° - \eta\|$ while the mass distribution over the wing surface is assumed to be uniform. For a given prescribed sweeping motion ϕ, the tuned elastic hinge stiffness fully determines the (passive) pitching motion and, therefore, the aerodynamic force generation (e.g.,

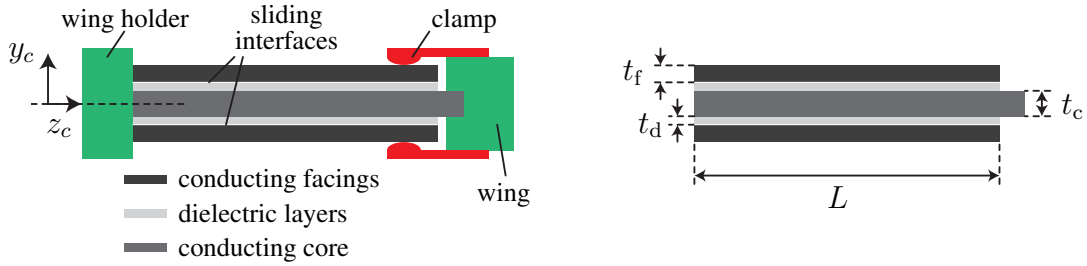

(a) Side-view symmetric active hinge. (b) Dimensions active hinge design.

Figure 3: Symmetric active hinge design.

lift force). Consequently, changing the elastic hinge stiffness in an active manner would lead to changes of the aerodynamic force generation and, hence, to a way to control FWMAV flight.

3 ELECTROSTATIC CONTROLLED HINGE THEORY

This section discusses a model to electrostatically control the dynamic properties of the active hinge. First, it presents the proposed hinge design followed by a description of the voltage-induced normal stress between the stacked layers. After that, we describe the voltage-dependent behavior during the flapping motion (i.e., whether the layers are sliding or being clamped). Then we show the voltage-dependent properties of the active hinge (i.e., its rotational stiffness and Coulomb friction) during the flapping motion. Finally, we present two reference hinge configurations.

3.1 Proposed elastic hinge design

The elastic hinge in the wing design of Figure 2 is replaced by an active hinge for which an enlarged side-view is shown in Figure 3a. The hinge is symmetric about the z_c-axis (i.e., in both pitching directions). The hinge has a length L and width b. This hinge consists of a conducting core which is surrounded by dielectric layers and two conducting facings. The core connects the wing holder to the wing while the two facings are attached to the wing holder only. The two facings can slide with respect to the core. The thickness of the core, the dielectric layers, and the facings are denoted by t_c, t_d, and t_f, respectively, see Figure 3b. Two clamps are attached to the wing to prevent the layers from separating during the pitching motion. The facings can freely slide with respect to the clamp. Hence, the bending stiffness of the active hinge is always determined by all layers.

3.2 Voltage induced stresses between stacked layers

An electric field is created over the dielectric layers by applying a voltage V to the conducting facings while the core is connected to ground. This electric field induces a normal stress which is given by

$$\sigma_N\left(V\right) = \frac{\varepsilon_0 \varepsilon_\mathrm{r} V^2}{2t_\mathrm{c}^2}, \tag{4}$$

where $\varepsilon_0 = 8.854 \times 10^{-12}$ F/m represents the vacuum permittivity and ε_r is the material dependent relative permittivity. Eq. (4) depends quadratically on the applied voltage V and inversely quadratic on the gap between the conducting layers (i.e., the dielectric layer thickness t_c). The normal stress can prevent the stacked layers from sliding by balancing the introduced shear stress at the interface during deflection. The maximum voltage dependent shear stress before the layers start sliding is

$$\tau_\mathrm{N}(V) = \mu \sigma_\mathrm{N}(V), \tag{5}$$

where μ represents the friction coefficient. The dynamic friction coefficient, μ_d, is, in general, lower compared to the static friction coefficient μ_s for engineering materials. Eq. (5) represents the shear stress threshold value and the stacked layers start sliding if the shear stress at the interface becomes higher than this value.

3.3 Principle behavior of hinge during large deformations

During the pitching motion, the active hinge is deflecting. We assume the stacked layers to slide without restriction for $V = 0$. For $V > 0$, the voltage induced normal stress tries to prevent the layers from sliding (i.e., clamps the layers together). The required normal stress to prevent the layers from sliding depends on the pitching angle η. V_cl denotes the required voltage to clamp the layers completely throughout the entire cycle.

Figure 4 shows conceptual steady-state clamping-sliding behavior of the active hinge during a pitching motion η for a voltage $0 < V < V_\mathrm{cl}$ with the corresponding shear stress τ_in at the interface $y_c = 0.5t_\mathrm{c} + t_\mathrm{d}$. At the start of the graph, η increases while the layers are sliding with respect to each other and the shear stress at the sliding interface is constant and equal to the voltage induced threshold shear stress (i.e., $\tau_\mathrm{N}(V)$). This interface shear stress causes a deformation of the layers, see State 1 in Figure 5. For $\dot{\eta} = 0$ (i.e., maximum pitching angle), sliding stops leaving an off-set between the hinge layers, see Configuration 1 in Figure 4.

At the start of the reversal stroke, η decreases and the stacked layers are clamped (i.e., $\tau_\mathrm{in} \leq \tau_\mathrm{N}(V)$) while the corresponding layer deformation changes can be represented by States 1 - 5 in Figure 5. The interface shear stress decreases according to η until $\tau_\mathrm{in} = -\tau_\mathrm{N}(V)$. At that point, the layers did not slide yet (i.e., Configurations 1 & 2 show the same off-set, see Figure 4). For a further decreasing η, the layers slide until $\dot{\eta} = 0$ at the maximum negative pitching angle. During that sliding, the hinge configuration changes (i.e., Configuration 2 to 3 in Figure 4) while the interface shear stress and, hence, the layer deformation is constant (i.e., States 5 - 7 in Figure 5).

This work assumes a linear relation between the interface shear stress and the pitching angle. During clamping, the interface shear stress changes from plus $\tau_\mathrm{N}(V)$ (e.g., State 1 of Figure 5) to minus $\tau_\mathrm{N}(V)$ (e.g., State 5 of Figure 5) if the pitching angle decreases (or, visa versa, from $-\tau_\mathrm{N}(V) \rightarrow \tau_\mathrm{N}(V)$ if η increases). This results a total change of the interface shear stress of $\Delta\tau_\mathrm{in} = 2\tau_\mathrm{N}(V)$. The relation between the interface shear stress change, $\Delta\tau_\mathrm{in}$, and the pitching

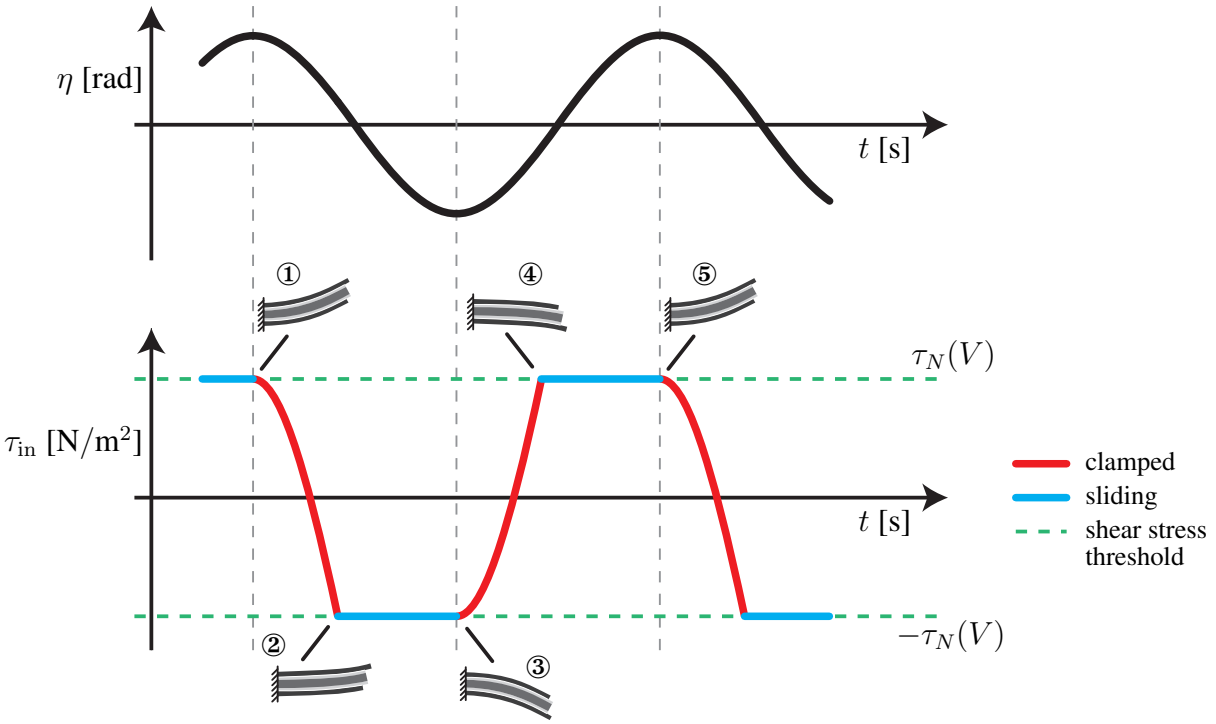

Figure 4: Conceptual steady-state clamping-sliding behavior of the voltage controlled active hinge during pitching η for a voltage $0 < V < V_{\text{cl}}$ with the corresponding shear stress τ_{in} at the interface $y_c = 0.5t_{\text{c}} + t_{\text{d}}$. Characteristic layer off-set configurations are indicated by Configuration 1 - 5.

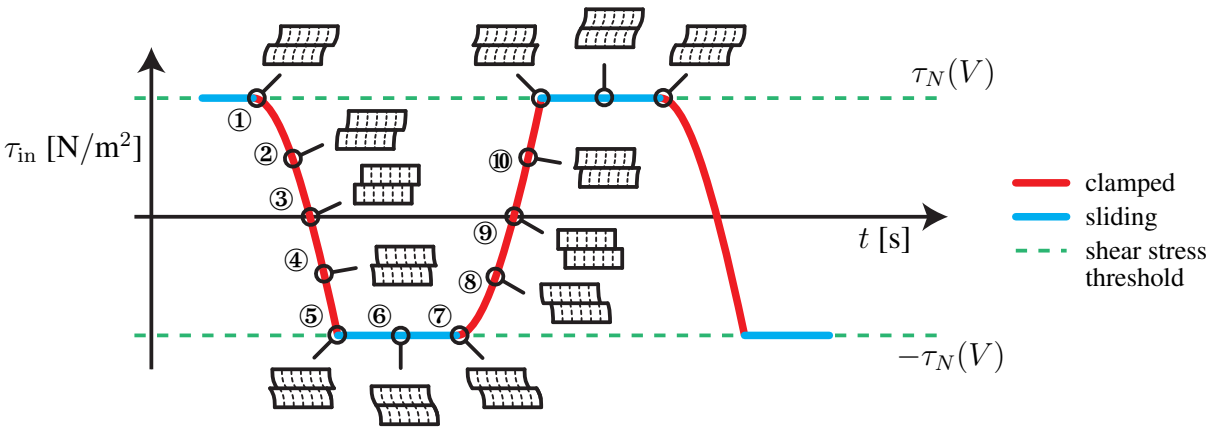

Figure 5: Conceptual sketches of layer deformation at different interface shear stress values of the voltage controlled active hinge during steady-state pitching η for a voltage $0 < V < V_{\text{cl}}$. States 1 - 10 represent characteristic deformation sketches.

amplitude difference, $\Delta\eta$, can be given by

$$\Delta\tau_{\text{in}}\left(z_c, y_c, \Delta\eta\right) = \Delta\tau_{\text{in}}\left(z_c, 0.5t_{\text{c}} + t_{\text{d}}, \Delta\eta\right) = \frac{\Delta P\left(z_c, \Delta\eta\right)}{Db}\sum\left(SE\right), \tag{6}$$

which is derived from sandwich beam theory [12]. In Eq. (6), D represents the flexural rigidity of the entire cross section, b gives the width of the active element at the interface, and $\sum(SE)$ represents the sum of the products of the first moment of area S and the Young's modulus E of the sandwich facing for $(0.5t_{\text{c}} + t_{\text{d}}) \leq y_c \leq (0.5t_{\text{c}} + t_{\text{d}} + t_{\text{f}})$. P denotes the shear force at the section of consideration. The change of this shear force, ΔP, is directly related to the pitching amplitude difference $\Delta\eta$ via the rotational stiffness, k_{rot}, of the stacked elastic hinge. Subsequently, we can determine the pitching amplitude difference, $\Delta\eta$, such that the interface shear stress changed by $2\tau_{\text{N}}(V)$ and the layers start sliding again after being clamped (e.g., Configuration 2 in Figure 4 and State 5 in Figure 5).

Thereafter, a similar but opposite cycle starts followed by identical consecutive cycles. If the stacked layers are clamped, the layer off-set remains the same (e.g., Configuration 3 & 4 are equal in Figure 4) while the shear stress at the interface and, hence, the layer deformation changes (e.g., States 7 - 10 in Figure 5). On the other hand, if the stacked layers are sliding, the hinge configuration changes (e.g., from Configuration 4 to 5 in Figure 4) while the shear stress at the interface remains constant with a magnitude of $\tau_{\text{N}}(V)$. The influence of the offset between the hinge layers during deflection and their corresponding complexity (e.g., buckling) is neglected. Additionally, the static and dynamic friction coefficient are assumed to be equal in the conceptual sketches of Figures 4 & 5.

3.4 Voltage-dependent hinge properties

The dynamic property changes of the active hinge as a function of the applied voltage are twofold: 1) rotational stiffness changes, and 2) energy dissipation changes due to Coulomb friction at the layers interface. Both influence the passive pitching response.

With respect to the rotational stiffness k_{rot}, two states can be distinguished:

1. clamped stiffness $k_{\text{rot}}^{\text{cl}}$, for which the stacked layers are clamped and the hinge consists, basically, of a single bending element with a weighted Young's modulus $\bar{E}$ and area moment of inertia $\bar{I}$, and

2. sliding stiffness $k_{\text{rot}}^{\text{sl}}$, for which the stacked layers rotate freely with respect to each other such that the hinge consists of three individually bending layers with a weighted Young's moduli $\bar{E}_{\text{c}}$ and area moment of inertia $\bar{I}_{\text{c}}$ for the conducting core with wrapped dielectric layers, and E_{f} and I_{f} for the facings.

The corresponding rotational stiffness is, consequently, given by

$$k_{\text{rot}}^{\text{cl}} = \frac{\bar{E}\bar{I}}{L}, \qquad \text{and} \qquad k_{\text{rot}}^{\text{sl}} = \frac{\bar{E}_{\text{c}}\bar{I}_{\text{c}}}{L} + 2\frac{E_{\text{f}}I_{\text{f}}}{L}, \tag{7}$$

respectively. The rotational stiffness of the clamped hinge is significantly higher compared to the sliding hinge. For a beam consisting of n stacked layers with equal dimensions and material properties, the ratio between the area moment of inertia in the case of clamped stacked layers is n^2 times higher compared to the area moment of inertia in the case of sliding stacked layers. Subsequently, the rotational stiffness is n^2 times higher.

For $0 < V < V_{\mathrm{cl}}$, the layers of the active hinge are sequentially clamped and sliding throughout the pitching motion. If the layers are sliding, energy will be absorbed via sliding friction resulting in a mechanical damping, which is assumed to be modeled as Coulomb friction. The friction force F_{fr} at the interface due to sliding is

$$F_{\mathrm{fr}}\left(V\right) = \mu_{\mathrm{d}} \sigma_{\mathrm{N}}\left(V\right) Lb, \tag{8}$$

which explicitly assumes that the friction force is equal to zero for $V = 0$ although this assumption oversimplifies the occurring sliding behavior due to the inevitable normal stress between layers which are jointly bending without being clamped. Eq. (8) additionally assumes sliding of the whole surface. The friction forces at the interface counteract the passive pitching motion of the wings. The counteracting moment due to the friction forces can be written by

$$M_{x_c}^{\mathrm{Cou}}\left(\dot{\eta}, V\right) = \begin{cases} 0 & \text{if} \quad V = 0, \\ 0 & \text{if} \quad \text{clamped}, \\ -\mathrm{sgn}\left(\dot{\eta}\right) \mu_{\mathrm{d}} \sigma_{\mathrm{N}}(V) Lb \left(t_{\mathrm{c}} + 2t_{\mathrm{d}} + t_{\mathrm{f}}\right) & \text{if} \quad \text{sliding}, \end{cases} \tag{9}$$

where $\mathrm{sgn}(\cdot)$ is the signum function. Hence, there is only a damping moment if the layers are sliding and the applied voltage is unequal to zero.

3.5 Reference configurations active hinge

There are basically two reference or starting configurations of the currently described active hinge to control the passive pitching motion:

1. The **sliding-mode** where $V_{\mathrm{ref}} = 0$ and $k_{\mathrm{rot}} = k_{\mathrm{rot}}^{\mathrm{sl}}$.
2. The **clamped-mode** where $V_{\mathrm{ref}} = V_{\mathrm{cl}}$ and $k_{\mathrm{rot}} = k_{\mathrm{rot}}^{\mathrm{cl}}$.

Both approaches are feasible to obtain an active hinge with electrostatically controlled dynamic properties. However, the following remarks need to be made: I) in practice, the inter-layer normal stress is most likely deviating from zero for $V = 0$ which leads to (undesirable) Coulomb friction, II) the dielectric strength of the isolation layer might be not high enough to allow for the required voltage V_{cl} to maintain full clamping throughout the pitching cycle (i.e., clamped-mode), III) the friction coefficient μ might change significantly during extensive cyclic loading due to wear. Despite these remarks, the description allows us to study the influence of an electrostatically controlled active hinge on the passive pitching motion of a flapping wing.

4 EQUATION OF MOTION OF PASSIVE PITCHING MOTION

The rigid wing model involves only one degree of freedom, the pitching η. The equation of motion that governs η can be obtained by applying Euler's second law of motion. That is,

$$M_{x_c}^{\text{applied}} + M_{x_c}^{\text{iner}} = 0, \tag{10}$$

where the inertial torque, $M_{x_c}^{\text{iner}}$, in the co-rotating frame is given by

$$M_{x_c}^{\text{iner}} = I_{x_c x_c}\left[\frac{1}{2}\sin(2\eta)\dot{\phi}^2 - \ddot{\eta}\right] - I_{x_c z_c}\ddot{\phi}\cos(\eta), \tag{11}$$

where $I_{x_c x_c}$ and $I_{x_c z_c}$ are moment of inertia terms. The applied torque, $M_{x_c}^{\text{applied}}$, acting around the pitching axis consists of three components: I) the elastic torque from the active hinge, $M_{x_c}^{\text{elas}}$, for which the rotational stiffness is given by Eq. (7), II) the voltage dependent torque due to Coulomb friction during sliding, $M_{x_c}^{\text{Cou}}$, as calculated with Eq. (9), and III) the aerodynamic torque $M_{x_c}^{\text{aero}}$.

A quasi-steady aerodynamic model is used to calculate the transient aerodynamic loads. This paper only shows the terms relevant for this work without going into much detail on the specific terms. For more details on this model the reader is referred to [13]. The aerodynamic model assumes the resultant aerodynamic force acting on the wing to be always perpendicular to the chord over the entire stroke (i.e., in y_c-direction). For thin plates, this assumption is justified due to negligible leading-edge suction force and wing surface viscous drag compared to the dominant pressure force. The loads are decomposed into four components that originate from different sources: 1) the wing translational velocity leading to $F_{y_c}^{\text{trans}}$ and $M_{y_c}^{\text{trans}}$ (see, for example, [14]), 2) the coupling effect between wing translational and rotational effect leading to $F_{y_c}^{\text{coupl}}$ and $M_{y_c}^{\text{coupl}}$, 3) the pure rotational velocity leading to $F_{y_c}^{\text{rot}}$ and $M_{y_c}^{\text{rot}}$, and 4) the added mass effect leading to $F_{y_c}^{\text{am}}$ and $M_{y_c}^{\text{am}}$ (see, for example, [15]). This decomposition is illustrated in Figure 6. The resultant aerodynamic loads can be calculated by

$$\begin{aligned} F_{y_c}^{\text{aero}} &= \underbrace{-\text{sgn}(\omega_{z_c})\frac{1}{6}\rho_{\text{f}} c R^3 c_{F_{y_c}^{\text{trans}}}(\omega_{y_c}^2 + \omega_{z_c}^2)}_{F_{y_c}^{\text{trans}}} + \underbrace{\text{sgn}(\omega_{y_c})\frac{3}{8}\pi\rho_{\text{f}} c^2 R^2 \omega_{x_c}\sqrt{\omega_{y_c}^2 + \omega_{z_c}^2}}_{F_{y_c}^{\text{coupl}}} \\ &\quad \underbrace{-\frac{1}{6}\rho_{\text{f}} c^3 R C^{\text{rot}}\omega_{x_c}|\omega_{x_c}|}_{F_{y_c}^{\text{rot}}} + \underbrace{\frac{\pi}{8}\rho_{\text{f}} c^2 R\left[-R(\alpha_{z_c} + \omega_{x_c}\omega_{yc}) - c\alpha_{x_c}\right]}_{F_{y_c}^{\text{am}}}, \text{ and} \\ M_{y_c}^{\text{aero}} &= \underbrace{-\text{sgn}(\omega_{z_c})\frac{1}{6}\rho_{\text{f}} c^2 R^3 c_{F_{y_c}^{\text{trans}}}\hat{z}_{cp}^{\text{trans}}(\omega_{y_c}^2 + \omega_{z_c}^2)}_{M_{y_c}^{\text{trans}}} + \underbrace{\text{sgn}(\omega_{y_c})\frac{3}{32}\pi\rho_{\text{f}} c^3 R^2 \omega_{x_c}\sqrt{\omega_{y_c}^2 + \omega_{z_c}^2}}_{M_{y_c}^{\text{coupl}}} \\ &\quad \underbrace{-\frac{1}{8}\rho_{\text{f}} c^4 R C^{\text{rot}}\omega_{x_c}|\omega_{x_c}|}_{M_{y_c}^{\text{rot}}} + \underbrace{\frac{\pi}{16}\rho_{\text{f}} c^3 R\left[-R(\alpha_{z_c} + \omega_{x_c}\omega_{yc}) - \frac{9}{8}c\alpha_{x_c}\right]}_{M_{y_c}^{\text{am}}}, \end{aligned} \tag{12}$$

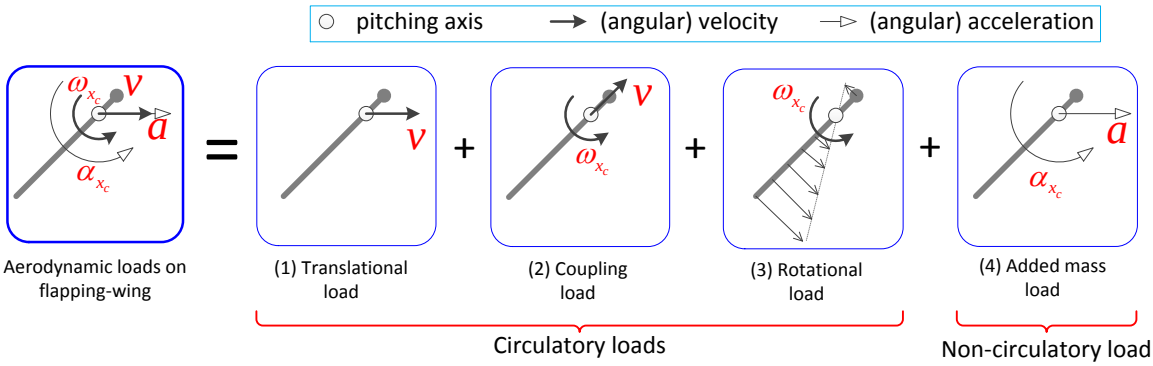

Figure 6: Decomposition of flapping wing aerodynamic loads as found using a quasi-steady aerodynamic model.

respectively, where ρ_{f} is the density of the fluid, R represents the wing span length, $\mathrm{sgn}(\cdot)$ is the signum function, $\hat{z}_{cp}^{\mathrm{trans}}$ is the position of the center of pressure due to the translational force which is calculated using an empirical formula (i.e., $\hat{z}_{cp}^{\mathrm{trans}} = 0.261\,(\mathrm{AOA}) + 0.05$), and C^{rot} is the drag coefficient for a plate revolving at an AOA of $90°$. We use an analytical model proposed by Taha *et al*. [16] to calculate the lift coefficient $c_{F_{yc}^{\mathrm{trans}}}$ due to the wing translational velocity. This analytical formula shows good prediction of lift coefficients of the translational flapping wing with different aspect ratios according to the comparison with those experimental data on bumble bee, fruit fly and hawk moth.

Eventually, the voltage dependent EoM of the wing passive pitching can be expressed as

$$I_{x_c x_c}\ddot{\eta} + k_{\mathrm{rot}}\eta = M_{y_c}^{\mathrm{aero}} + f(\eta, \dot{\eta}, V), \tag{13}$$

where the inertial drive torque $f(\eta, \dot{\eta}, V)$ is given by

$$f(\eta, \dot{\eta}, V) = \frac{1}{2} I_{x_c x_c}\dot{\phi}^2 \sin(2\eta) - I_{x_c z_c}\ddot{\phi}\cos(\eta) + M_{x_c}^{\mathrm{Cou}}(\dot{\eta}, V)\,. \tag{14}$$

Finally, Eq. 12 will be used to estimate the average lift generation by the flapping-wing with actively controlled elastic hinge.

5 EXPERIMENTAL SETUP

To validate the presented method on changing the dynamic properties of the wings' hinge using electrostatic clamping, experiments are done. First, we discuss the manufactured active wing and complete experimental setup. After that, we show the change of the passive pitching motion due to different applied voltages. Finally, we compare the experimentally and analytically obtained results.

5.1 Realization wing with active hinge

The wing design consists of three parts: I) the wing planform, II) the active hinge at the wingroot, and III) the wing holder, see Figure 7. The first part, the wing planform, is composed

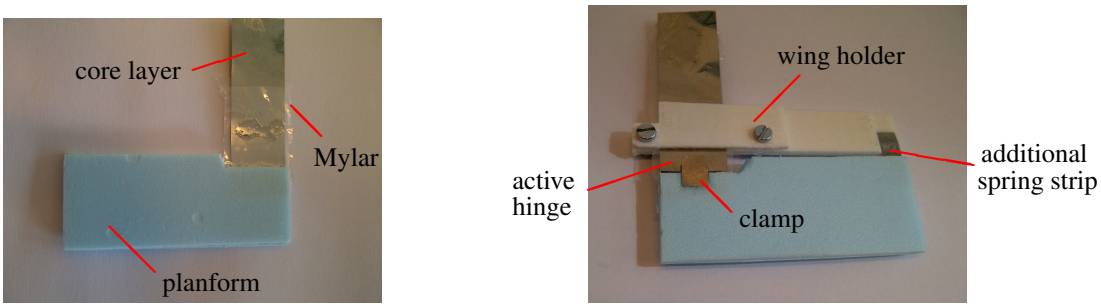

(a) Planform with wrapped core layer. (b) Realized wing design.

Figure 7: Wing design consisting of: I) the wing planform, II) the active hinge, and III) the wing holder.

by gluing two rectangular, 1 mm thick sheets of blue foam (i.e., Expanded PolyStyrene (EPS)) on top of each other. The wingspan $R = 50$ mm and its chord length $c = 20$ mm. The core layer of the active hinge is clamped between these two sheets. The resulting wing planform is relatively rigid compared to the compliance of the active hinge.

The second part, the active hinge, consists of a conducting core which is on both sides covered by, consecutively, a dielectric layer and a conducting facing. For all conducting layers, we use spring steel strips (i.e., Young's modulus $E = 210$ GPa). These spring steel strips are tough, have low fatigue, and allow for a large number of cyclic, large deflections. The strips have a width b of 12.7 mm and the thickness of the core and the facings is 20 μm and 5 μm, respectively. For the dielectric layers two different approaches can be followed: 1) spin coat a thin polymeric film unto the conducting layer(s) (e.g., the photo-resist SU-8), or 2) use thin sheets of dielectric polymer film (e.g., Mylar). In this work, 5 μm thick Mylar films are tightly attached to the core conducting layer, see Figure 7a. Its Young's modulus $E = 4.25$ GPa, the dielectric constant $\varepsilon_r = 3.25$, the static and dynamic friction coefficients with respect to steel are assumed to be equal, that is, $\mu_s = \mu_d = 0.2$[1], and the dielectric strength is $V_\mathrm{d} = 500$ V/μm [17, 18]. The total length of the active hinge $L = 5$ mm. To prevent the layer from separating during the pitching motion, clamps are added on both sides.

The third part, the wing holder, is made from 3D printed plastic. The wing holder is extended over the entire wing span to constrain the movement of the wingtip via a strip of spring steel with a relatively high bending compliance. This constraint prevents warping of the active hinge during large deflections which would lead to undesired large deflections in spanwise direction. The resulting wing design is shown in Figure 7b.

The total mass of the realized wing (excluding the wing holder) is around 300 mg which is relatively high compared to wings found in nature with similar dimensions (e.g., 50 mg) due to glue and the additional clamps. With the currently used layer thicknesses, the ratio between the bending stiffness in the clamped situation, $k_\mathrm{rot}^\mathrm{cl}$, and the sliding situation, $k_\mathrm{rot}^\mathrm{cl}$, is 2.34.

[1] Since we did not find appropriate information about the friction coefficient between Mylar (PET, Polyethylene terephthalate) and spring steel, we used the friction coefficient between the similar material PE (Polyethylene) and steel instead.

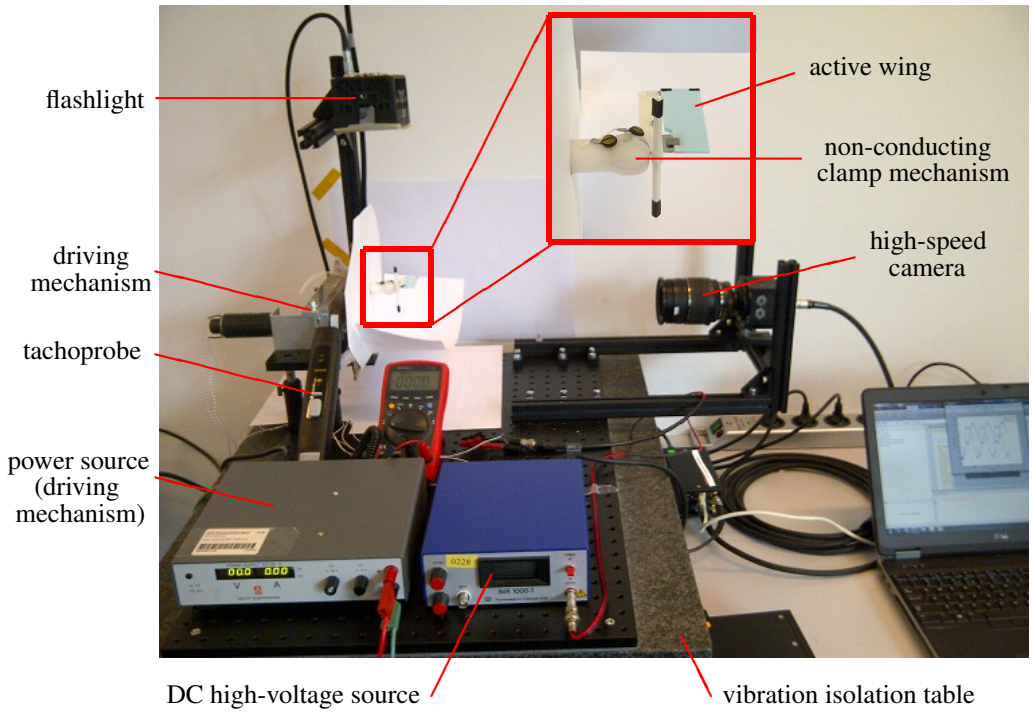

Figure 8: Experimental setup indicating the key components.

5.2 Experimental setup

Figure 8 shows a picture of the experimental setup as positioned on a vibration isolating table. The key components of this setup are: 1) the active wing, 2) a non-conducting clamping mechanism to apply the voltage to the facings and to ground the core layer, 3) a DC high-voltage source to apply the voltage to the active hinge, 4) a driving mechanism to enforce a harmonic sweeping motion to the wing, 5) a tachoprobe to measure the driving frequency, and 6) a high-speed camera with a flashlight to capture the flapping motion. Black markers are added to the wing design to allow for proper post-processing of the images captured by the camera.

5.3 Measurements and results

This section shows experimental results of one specific wing design. Although similar trends were found for other wing designs, this design shows the trend most clearly over a large range of applied voltages. Due to wing fabrication complications it was difficult to compare different designs over a large range of applied voltages. These complications were, among others, difficulties to handle the extremely thin spring steel and Mylar sheets (i.e., 5 μm) and challenges to prevent an additional air layer between the stacked layers. An additional air layer has a negative influence on the normal stress due to the applied voltage (see Eq. (4)). Hence, the number of well succeeded wing designs was limited.

The driving frequency was constant for all experiments and restricted to 12.5 Hz to prevent

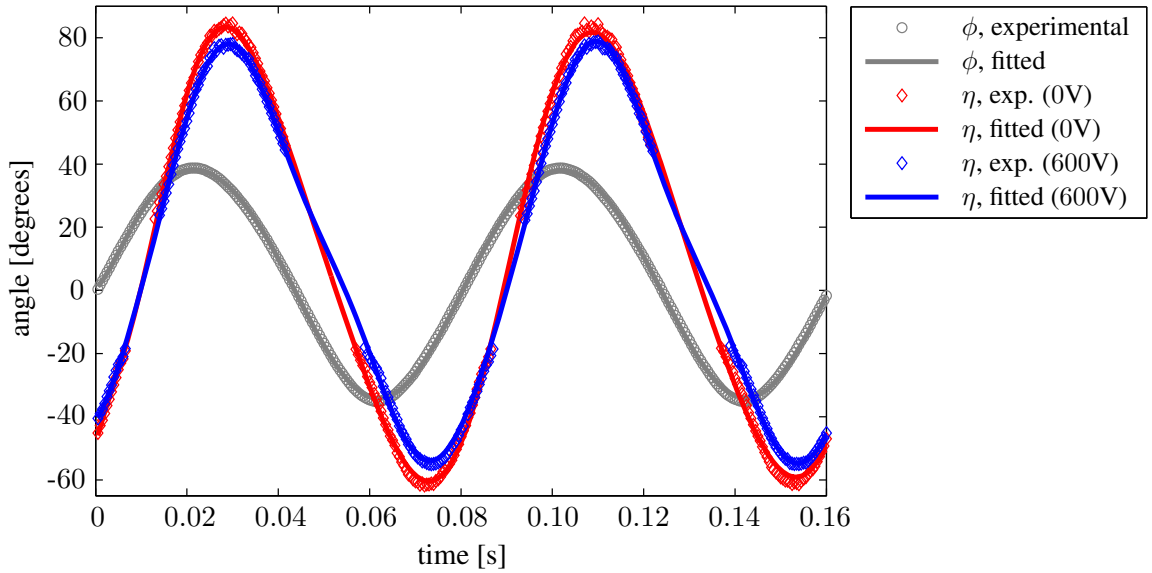

Figure 9: Flapping kinematics of a passive pitching wing design for which the pitching amplitude decreases if the applied voltage to the active hinge increases.

large pitching amplitudes (i.e., > 90 degrees). Figure 9 shows the resulting flapping kinematics: the sweeping motion ϕ and the passive pitching motion η. The passive pitching motion lags behind the sweeping motion by about 30 degrees. The amplitude of the sweeping motion ϕ is 37.5 degrees. The maximum passive pitching angle decreases if the applied voltage to the active hinge increases (i.e., the maximum pitching angle decreases from about 84 degrees for 0 V to about 78 degrees for 600 V) and the phase lag becomes slightly bigger (i.e., a few degrees). The asymmetry of the passive pitching motion is caused by inaccuracies of the realized flapping wing design. The small irregularities or disappearance of measurement points for the pitching motion is caused by the difficulties in tracking the markers on the flapping wing, especially around $\eta = 0$ degrees.

Figure 10 shows the change of the average pitching amplitude (using both the maximum and minimum pitching angle) as a function of the applied voltage to the active hinge. To get these results, the flapping frequency was fixed to 12.5 Hz and the applied voltage was increased in steps of 100 V to the maximum of 600 V. For each measurement point, we waited a few seconds to be assured of steady-state motion before taking images. The error bars around the measurement points are introduced by post-processing the images for which the process is prone to errors due to the present manual operations.

Figure 10 shows an increase of the average passive pitching amplitude up to 200 V followed by a monotonic decrease of this amplitude for higher voltages. A possible explanation for this initial amplitude increase is the presence of the clamps on the wings to keep the layers from separating. The friction between these clamps and the outer facings of the active hinge decreases if the voltage increases which reduces the energy loss and, hence, increases the average pitching amplitude.

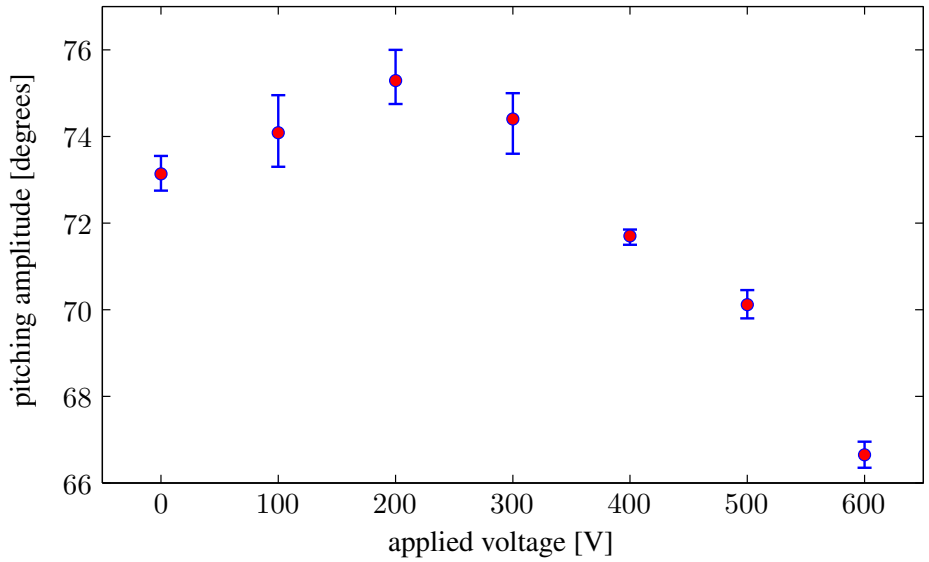

Figure 10: Average pitching amplitude and corresponding error bars due to image post-processing as a function of the applied voltage to the active hinge.

The targeted gap between the core conducting layer and the outer facings was $5\ \mu$m as determined by the thickness of the Mylar sheet. Since the electric strength of Mylar is $500\ \mathrm{V}/\mu$m, the maximum possible applied voltage to the active hinge is, theoretically, restricted to 2500 V. The Figures 9 and 10 show only results up to 600 V since the hinge failed for higher voltages. This could have several reasons, for example: I) due to Mylar sheet irregularities (e.g., a small scratch) the practical dielectric strength is lower than the theoretical dielectric strength, or II) due to the presence of a very thin air gap between the conducting layers and the dielectric sheet. If the breakthrough voltage of the air gap is reached, a current is going to flow which might locally burn the dielectric Mylar layer. These reasons complicate the calculation of the normal stress (see Eq. (4)) to clamp the layers and the friction force (Eq. (8)) at the interface and, hence, a proper estimation of the pitching amplitude change due to the applied voltage.

5.4 Numerical analysis and comparison to experimental results

Figure 11 shows analytical steady-state sweeping ϕ and passive pitching η for different applied voltages to the active hinge. The passive pitching motion without voltage (i.e., 0 V) lags behind the sweeping motion by about 30 degrees, which is comparable to the experimental results. The figure indicates the locations at which the layers are clamped during the cycle just after the maximum pitching angle is reached. The region of clamping increases if the applied voltage increases but this region remains relatively small with respect to the entire flapping cycle. The ode15s solver from Matlab is used to solve this stiff problem due to the sudden changes of the hinge stiffness if the layers are clamped together. The figure clearly shows the decrease in the pitching amplitude for an increase of the voltage. Additionally, we see an increase of the phase lag between the passive pitching and the sweeping motion.

Figure 12a shows the analytical change of the average pitching amplitude as a function of

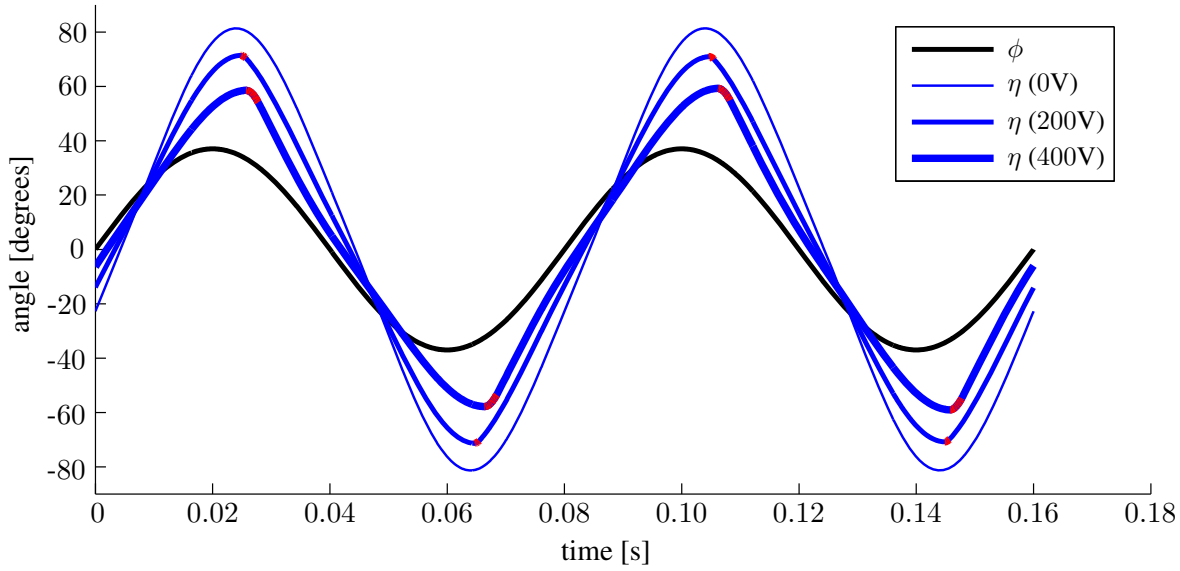

Figure 11: Numerical results of the flapping kinematics for different applied voltages to the active hinge. The figure also indicates the location during the cycle (i.e., just after the maximum pitching angle) at which the layers are clamped together.

the applied voltage to the active hinge. The maximum applied voltage is set to 400 V. If the applied voltage becomes higher than 400 V, the passive pitching motion of Figure 11 starts to deviate significantly from a harmonic motion due to nonlinearity of the equation of motion that governs the passive pitching motion. The average pitching angle decreases monotonically, almost linearly, if the voltage increases. The cycle-average lift force decreases accordingly, see Figure 12b. The average lift force decreases by about 32 % if the voltage is increased from 0 V to 400 V which allows active flight control of FWMAVs.

The analytical passive pitching amplitude change due to the applied voltage (i.e., Figures 11 and 12) is more significant compared to the experimental results of Figures 9 and 10

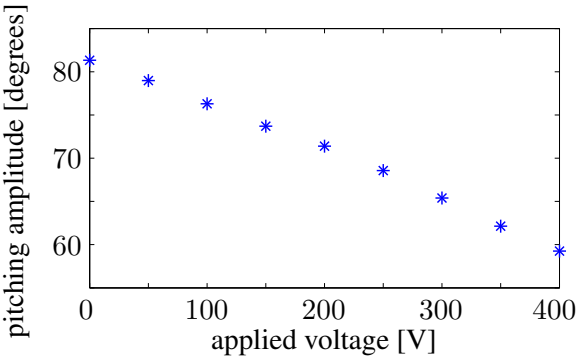

(a) Average passive pitching amplitude as a function of the applied voltage.

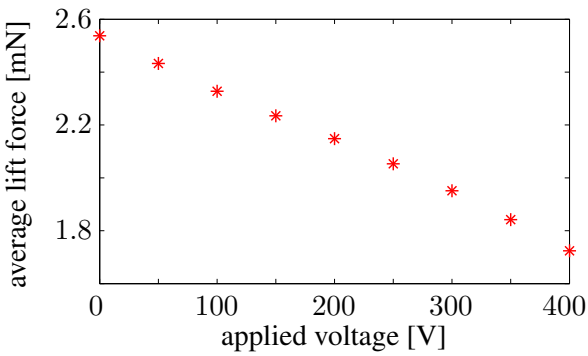

(b) Average lift force as a function of the applied voltage.

Figure 12: Analytical change of the passive pitching amplitude and the average lift force as a function of the applied voltage to the active hinge.

although the trend is similar (i.e., decreased amplitude and increased phase different for an increasing actuation voltage). The difference between the analytical and experimental results can be explained by: 1) the simplifying assumptions in the theoretical model, 2) the difficulties in the manufacturing process, and 3) the presence of additional air between the conducting layers.

6 CONCLUSIONS AND RECOMMENDATIONS

This paper presents a method to actively control the passive pitching motion of a flapping wing using the clamping of stacked layers via an electrostatic loading. These stacked layers constitute the elastic hinge at the wing root in a FWMAV design. Actively controlling the structural properties (e.g., damping and stiffness) of that hinge results in significant changes of the wings' passive pitching motion and, hence, of its lift production. This work uses a hinge which consists of three conducting spring steel layers which are separated from each other by two dielectric Mylar films.

During the pitching motion, the layers are, consecutively, clamped and sliding with respect to each other. The layers are clamped by the voltage induced normal stress between the layers. During clamping, the bending stiffness of the hinge is significantly higher compared to the case when the layers are sliding (i.e., $2.34\times$ for our hinge). When the layers are sliding, however, there is Coulomb friction between the sliding layers due to the normal stress between the layers as induced by the applied voltage. This Coulomb friction causes an additional moment on the hinge which counteracts the passive pitching motion.

Numerical simulations show significant changes of the pitching amplitude if the actuation voltage to the active hinge increases. The duration of the clamped phase increases with the applied voltage, although it is relatively short compared to the sliding phase. The average lift changes corresponding to different applied voltages are sufficient to allow for FMWAV control purposes. The model gives, despite the introduced assumptions, a clear insight of the clamping-sliding phenomena of the active hinge, if the applied voltage increases.

Experiments are conducted to study the practical applicability of this active elastic hinge for small-scale and lightweight FWMAV applications. For experimental results, several fabrication difficulties had be tackled, for example, the handling of the very thin Mylar films (i.e., $5\ \mu$m). The experimentally obtained pitching amplitude differences are reduced by the presence of an air layer between the conducting layers and the dielectric layers and due to present irregularities of the Mylar film. Despite these short-comings, the results clearly show a decrease of the pitching amplitude as a function of the applied voltage. Hence, it shows the feasibility of this method to control FWMAVs.

In future work, the analytical model might be improved to model the clamping-sliding behavior more accurately (e.g., the relation between pitching angle and interface shear stress). Additionally, long lasting experiments need to be conducted to study the influence of wear on the friction coefficient between the Mylar and the conducting sheets. Alternatively, it is interesting to change the activation voltage during a flapping cycle and study the occurring transient behavior. The fabrication process can be optimized by preparing jigs or well-designed tools. Additionally, the image post-processing can be improved to decrease the corresponding error.

ACKNOWLEDGEMENTS

This work is part of the Atalanta project from Cooperation DevLab and is supported by Point One - UII as project PNU10B24, Control of Resonant Compliant Structures. This work is also financially supported by Chinese Scholarship Council. We would like to thank the technical staff of PME for their support with the experimental setup.

References

[1] R. J. Wood. The first takeoff of a biologically inspired at-scale robotic insect. *IEEE Transactions on Robotics*, 24(2):341–347, 2008.

[2] C. T. Bolsman, J. F. L. Goosen, and F. van Keulen. Design overview of a resonant wing actuation mechanism for application in flapping wing mavs. *International Journal of Micro Air Vehicles*, 1(4):263–272, 2009.

[3] Z. E. Teoh, S. B. Fuller, P. Chirarattananon, N. O. Prez-Arancibia, J. D. Greenberg, and R. J. Wood. A hovering flapping-wing microrobot with altitude control and passive upright stability. In *IEEE International Conference on Intelligent Robots and Systems*, pages 3209–3216, 2012.

[4] B. M. Finio and R. J. Wood. Open-loop roll, pitch and yaw torques for a robotic bee. In *IEEE International Conference on Intelligent Robots and Systems*, pages 113–119, 2012. art. no. 6385519.

[5] K. Y. Ma, S. M. Felton, and R. J. Wood. Design, fabrication, and modeling of the split actuator microrobotic bee. In *IEEE International Conference on Intelligent Robots and Systems*, pages 1133–1140, 2012. art. no. 6386192.

[6] Z. E. Teoh and R. J. Wood. A bioinspired approach to torque control in an insect-sized flapping-wing robot. In *Proceedings of the IEEE RAS and EMBS International Conference on Biomedical Robotics and Biomechatronics*, pages 911–917, 2014. art. no. 6913897.

[7] C. Majidi and R. J. Wood. Tunable elastic stiffness with microconfined magnetorheological domains at low magnetic field. *Applied Physics Letters*, 97(16), 2010. art. no. 164104.

[8] W. W. Clark. Vibration control with state-switched piezoelectric materials. *Journal of Intelligent Material Systems and Structures*, 11(4):263–271, 2000.

[9] O. Tabata, S. Konishi, P. Cusin, Y. Ito, F. Kawai, S. Hirai, and S. Kawamura. Micro fabricated tunable bending stiffness devices. *Sensors and Actuators, A: Physical*, 89(1-2):119–123, 2001.

[10] A. Bergamini, R.X. Christen, B. Maag, and M. Motavalli. A sandwich beam with electrostatically tunable bending stiffness. *Smart Materials and Structures*, 15(3):678–686, 2006.

[11] L. L. Howell. *Compliant Mechanisms*. Wiley, 2001.

[12] H.G. Allen. *Analysis and Design of Structural Sandwich Panals*. Oxford: Pergamon Press, 1969.

[13] Q. Wang, J. F. L. Goosen, and F. van Keulen. Study of design parameters of flapping-wings. In *IMAV 2014: International Micro Air Vehicle Conference and Competition 2014*. Delft University of Technology, 2014. Delft, The Netherlands, August 12-15, 2014.

[14] S. P. Sane and Dickinson M. H. The aerodynamic effects of wing rotation and a revised quasi-steady model of flapping flight. *Journal of Experimental Biology*, 205(8):1087–1096, 2002.

[15] J.N. Newman. *Marine Hydrodynamics*. The MIT Press, 1977.

[16] H. E. Taha, M. R. Hajj, and P. S. Beran. State-space representation of the unsteady aerodynamics of flapping flight. *Aerosp. Sci. Technol.*, 34:1–11, 2014.

[17] Free Flight Supplies, April 2015. `www.freeflightsupplies.co.uk/mylarspec.pdf`.

[18] The Engineering Toolbox, April 2015. `http://www.engineeringtoolbox.com/friction-coefficients-d_778.html`.